Co-precipitation synthesis of $CuCo_2O_4$ nanoparticles for supercapacitor electrodes with large specific capacity and high rate capability

Mengxuan Sun[a], Qisheng Fang[a], Zhijie Li[a,*], Chao Cai [a], Hao Li[a], Baobao Cao[b], Wenzhong Shen[c], Terence Xiaoteng Liu[d], YongQing Fu[d,*]

[a] School of Physics, University of Electronic Science and Technology of China, Chengdu, 610054, P. R. China

[b] Key Laboratory of Advanced Technologies of Materials, Ministry of Education, Southwest Jiaotong University, Chengdu 610031, PR China

[c] State Key Laboratory of Coal Conversion, Institute of Coal Chemistry, Chinese Academy of Science, Taiyuan, 030001, P. R. China

[d] Faculty of Engineering and Environment, Northumbria University, Newcastle Upon Tyne, NE1 8ST, UK

Zhijie Li (**Corresponding Author**): ORCID: 0000-0001-9870-9939;

*E-mail: zhijieli@uestc.edu.cn; TEL: +86 02883202160

Yongqing Fu (**Corresponding Author**): ORCID: 0000-0001-9797-4036;

*E-mail: Richard.fu@northumbria.ac.uk; TEL: +44 (0)191 2274662

Abstract

Ultra-fine $CuCo_2O_4$ nanoparticles were synthesized using a facile co-precipitation method assisted by $NaBH_4$ and CTAB, and they were explored as supercapacitor electrode material to achieve a large specific capacity and a high rate capability. The synthesized $CuCo_2O_4$-250 nanoparticles had a large surface area of 159.6 $m^2\ g^{-1}$, which provided numerous active sites to enhance their specific capacity. The abundant mesopores with a pore volume of 0.3599 $cm^3\ g^{-1}$ effectively provided numerous channels for the electrolyte ions to diffuse onto the active surface of nanoparticles. The $CuCo_2O_4$-250 nanoparticles based electrodes exhibited both battery-type and capacitive-type behavior in the charging/discharging processes. It achieved a large specific capacity of 401.2 C g^{-1} at a current density of 0.5 A g^{-1} in 2 M KOH electrolyte. Results showed that when the current density was increased from 1 A g^{-1} to 10 A g^{-1}, a retained specific capacitance of 77.5% was achieved, indicating a good rate capability. An asymmetric supercapacitor with $CuCo_2O_4$-250 nanoparticles and activated carbon as positive and negative electrodes exhibited a high energy density of 29.5 Wh kg^{-1} at a power density of 832.6 W kg^{-1} and a capacity retention of 72.7 % at 10 A g^{-1} after 10000 cycles.

Key words: $CuCo_2O_4$, Nanoparticles, Co-precipitation, Electrochemical, Supercapacitor.

1 Introduction

To tackle the problems of decreasing fossil fuel and serious environmental pollution, it is urgently required to develop highly efficient and clean energy storage technologies. Supercapacitors (SCs) are one of the promising candidates and have attracted great attention in recent years due to their high cyclability, fast charging speed, high rate capability, high power density, friendly environmental feature and safe operation [1]. Various types of materials have been investigated as active electrode materials for the SCs, such as carbon materials [2], conducting polymers [3], metal oxides or hydroxides [4, 5] and metal sulfides [6]. Metal oxides generally have larger specific capacitances than those of carbon materials and conducting polymers. Especially, ternary metal oxides, including $NiCo_2O_4$ [7, 8], $CuCo_2O_4$ [9], $MnCo_2O_4$ [10, 11] and $ZnCo_2O_4$ [12-14] have abundant electrochemical active sites, high theoretical capacitances and low cost. Therefore, they have been regarded as the promising electrode materials for SCs.

Among these ternary metal oxides, nanostructured $CuCo_2O_4$ has been reported to exhibit excellent electrochemical performance due to its various valence states from different metal ions, and its nanostructures include nanowires [15], nanoneedle arrays [16, 17], ordered corn-like nanoforests [18], cedar leaf-like, nanourchin [19], nanoflowers [20], nanosheets [21, 22], nanoparticles [23-25], microsphere-like nanosheets [26]. However, the $CuCo_2O_4$ based electrodes often exhibit a low rate capability. Most of these $CuCo_2O_4$ electrode materials with superior capacitance values are generally grown directly onto substrates of current collectors (e.g. nickel foam, graphite paper or carbon fabric) [20, 22, 27-29]. The electrodes fabricated by coating

nickel foam using as-prepared $CuCo_2O_4$ powders often showed low values of specific capacitances. For example, the $CuCo_2O_4$ nanoneedle arrays [30] showed a specific capacitance of 390 F g^{-1} at a current density of 0.5 A g^{-1} with a rate capability of 38.5 % for 10 A g^{-1}. Triple-shelled and hollow $CuCo_2O_4$ microspheres [31] exhibited a specific capacitance of 691 F g^{-1} at 1 A g^{-1} and retained 470 F g^{-1} at 20 A g^{-1}, with a rate capability of 68 %. Hierarchical $CuCo_2O_4$ nanoflowers [32] showed a capacity of 202.8 C g^{-1} at 1 A g^{-1}, which could retain about 48 % at 10 A g^{-1}. $CuCo_2O_4$ nanoparticles [33] had a capacity of 206 C g^{-1} at 0.4 A g^{-1}, which was decreased to 66 C g^{-1} at 2 A g^{-1}. Obviously these specific capacitance values and rate capability obtained using these $CuCo_2O_4$ nanostructured electrodes need to be significantly improved. Therefore, it is still a great challenge to explore different $CuCo_2O_4$ nanostructures with large specific capacitance and high rate capability. In addition, $CuCo_2O_4$ nanostructures were mostly synthesized using hydrothermal [9, 33], electrospinning [27] and electrodeposition methods [21, 22]. However, these methods are often complex and energy-consuming. Therefore, it is desired to develop a facile and energy-efficient method to prepare $CuCo_2O_4$ nanomaterials with superior supercapacitor properties.

In this work, ultra-fine $CuCo_2O_4$ nanoparticles were synthesized using a co-precipitation method assisted by sodium borohydride ($NaBH_4$) and hexadecyl trimethyl ammonium bromide (CTAB). The supercapacitor electrodes were then fabricated by coating these $CuCo_2O_4$ nanoparticles onto a nickel foam, and they showed a high specific capacity and good rate capability. An asymmetric supercapacitor (ASC) were fabricated by assembling the $CuCo_2O_4$ nanoparticles as the positive electrode and

activated carbon (AC) as the negative electrode, and exhibited a good electrochemical performance.

2 Experimental details

2.1 Preparation of $CuCo_2O_4$ nanoparticles

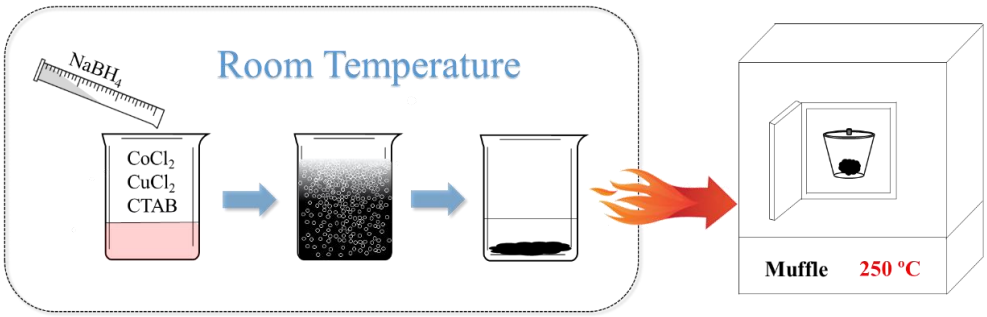

Fig.1 Schematic illustration of synthesis process of $CuCo_2O_4$ nanoparticles.

Fig. 1 shows the synthesis process of $CuCo_2O_4$ nanoparticles. At room temperature, 1.8223 g of CTAB, 0.7138 g of $CoCl_2 \cdot 6H_2O$ and 0.1705 g of $CuCl_2 \cdot 2H_2O$ were added into 100 ml of deionized water and stirred for 10 min. Then, 5 ml of $NaBH_4$ solution (2 mol/L) was added into the above solution under stirring, and lots of bubbles were generated. It was stirred for another 30 minutes until the bubbles were disappeared and a non-transparent black sol was formed. Black nanoparticles were precipitated from the sol after 6 hours. They were then collected by centrifugation, and washed with a mixed solution of water and alcohol for three times. Finally, they were dried at 60 ºC for 12 hours and marked as $CuCo_2O_4$-60. The $CuCo_2O_4$-60 was heat-treated at 250 ºC and 450 ºC in air for 2 hours to obtain the $CuCo_2O_4$ nanoparticles, which were marked as $CuCo_2O_4$-250 and $CuCo_2O_4$-450, respectively.

2.2 Materials characterization

Crystalline structures and phases of the samples were characterized using an X-ray diffractometer (XRD, Rigaku D/max-2400) with a Cu Kα radiation, α=0.15406 nm. Morphology, crystallinity and chemical composition of the samples were analyzed using a high-resolution transmission electron microscope (HRTEM, JEOL JEM-2100F), equipped with an energy-dispersive X-ray spectroscope (EDS). Chemical states of elements were characterized using an X-ray photoelectron spectrometer (XPS, Kratos Axis-Ultra DLD) with an Al Kα radiation. The specific surface areas and pore structure of samples were analyzed by N_2 adsorption-desorption method using Micromeritics ASAP2460 instrument and the specific surface area was calculated by Brunauer–Emmett–Teller (BET) method. Pore size distribution and pore volume were calculated using the Barrett–Joyner–Halenda (BJH) method.

2.3 Electrochemical characterization

The active materials of $CuCo_2O_4$ nanoparticles, binder of polytetrafluoroethylene (PTFE) and conductive additive of carbon black were ultrasonically mixed in anhydrous ethyl alcohol to obtain a slurry, in which the mass ratio of $CuCo_2O_4$, PTFE and carbon black were 8:1:1. The slurry was dropped onto a cleaned nickel foam (with an area of 1 cm^2 and a thickness of 1 mm), and dried at 50 ºC in a vacuum oven for 10 hours. It was then pressed at a pressure of 10 MPa for 1 min to be used as the working electrode. The mass per unit area of $CuCo_2O_4$ samples coated on electrode was 1.68 mg cm^{-2}. The electrochemical properties were characterized on a three-electrode cell system with a counter electrode of platinum foil and an Hg/HgO reference electrode in an aqueous electrolyte of 2 mol/L KOH solution. Electrochemical impedance

spectroscopy (EIS) analysis was performed using an open circuit voltage with a 5 mV amplitude over a frequency range of 0.01 Hz ~ 100 kHz. All the measurements were performed using an electrochemical workstation (CHI660E, Shanghai Chenhua Instrument Co., China). For the assembly of the asymmetric supercapacitor device of two-electrode simulation cells, the $CuCo_2O_4$ nanoparticles and active carbon (AC) on nickel foams were applied as positive and negative electrodes, respectively, and a 2 mol/L KOH solution was used as the electrolyte. A mass loading ratio of $CuCo_2O_4$ dots (m_+) and AC (m_-) was calculated based on the charge balance theory according to the following equation [34]:

$$\frac{m_+}{m_-} = \frac{C_- \times \Delta V_-}{C_+ \times \Delta V_+} \quad (1)$$

where m_+ and m_- are the mass (mg) of $CuCo_2O_4$ and AC respectively, C_+ and C_- are the specific capacitance (F g^{-1}), ΔV_+ and ΔV_- are potential windows (V) in the charge/discharge process for the positive ($CuCo_2O_4$) and negative (AC) electrodes, respectively.

3 Results and discussion

3.1 Electrochemical performance of $CuCo_2O_4$ samples

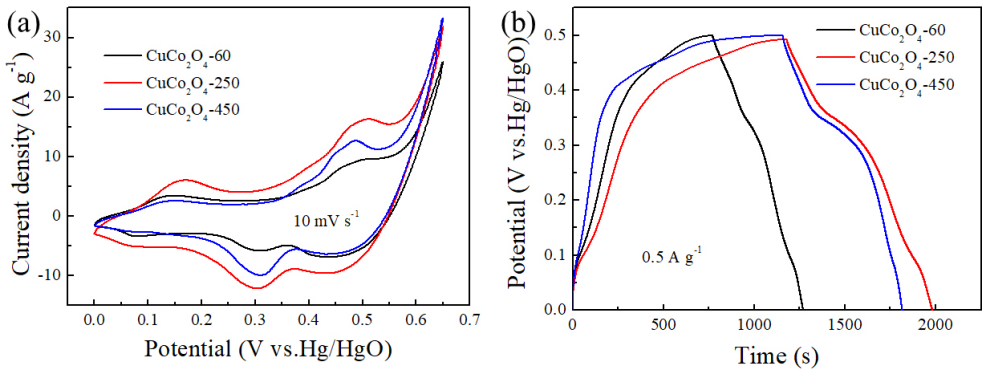

Fig. 2 (a) CV curves at the scan rate of 10 mV s^{-1} and (b) GCD curves at the current

density of 0.5 A g^{-1} of $CuCo_2O_4$ samples

Cyclic voltammogram (CV) curves of $CuCo_2O_4$ samples at 10 mV s^{-1} were measured in a 2 mol/L KOH aqueous electrolyte and the results are shown in Fig. 2a. In these CV curves, the closed area of the $CuCo_2O_4$-250 is larger than those of the $CuCo_2O_4$-60 and $CuCo_2O_4$-450, indicating that the $CuCo_2O_4$-250 has the largest specific capacity. The energy storage behaviors of the $CuCo_2O_4$ electrodes can be further proved by the curves of galvanostatic charge-discharge (GCD). As shown in Fig 2b, according to the discharge time (Δt, s), discharge current (I, mA) and potential window (ΔV, V) in the GCD curves and the mass of $CuCo_2O_4$ (m, mg) on electrode, the specific capacity value (C_s, C g^{-1}) can be calculated using the following formula (2) [9]. The specific capacity value of $CuCo_2O_4$-250 at 0.5 A g^{-1} is 401.2 C g^{-1}, which is larger than these of $CuCo_2O_4$-60 (248.8 C g^{-1}) and $CuCo_2O_4$-450 (329.3 C g^{-1}) indicating that $CuCo_2O_4$-250 has a better electrochemical performance. Therefore, the $CuCo_2O_4$-250 sample will be investigated in details in the sections.

$$C_s = \frac{I \times \Delta t}{m} \tag{2}$$

3.2 Characterization of $CuCo_2O_4$-250 sample

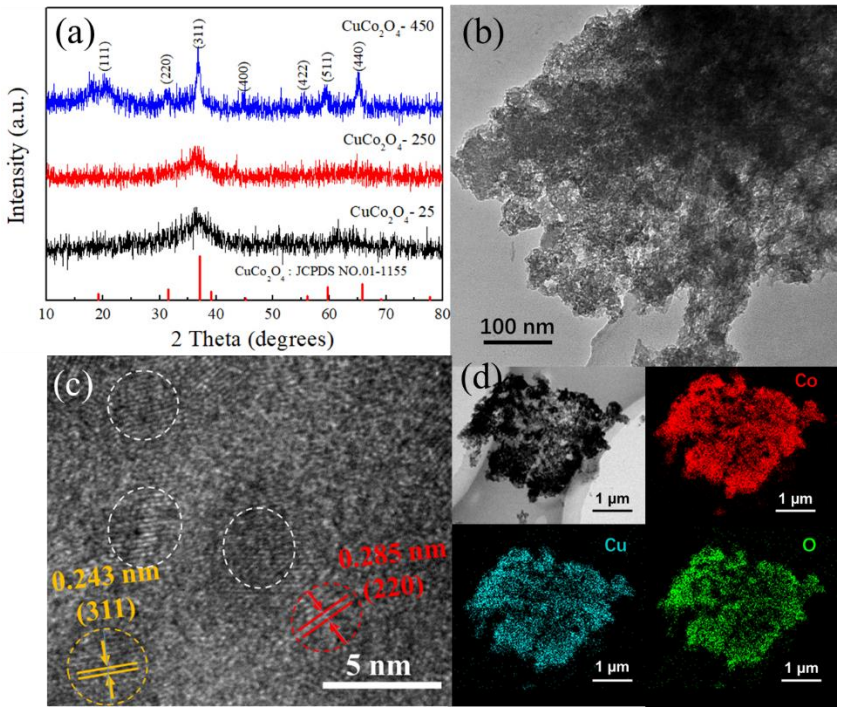

Fig. 3 (a) XRD spectra of $CuCo_2O_4$ samples, (b) TEM, (c) HR-TEM image and (d) EDX elemental mapping of $CuCo_2O_4$-250 sample.

Fig. 3a shows the XRD spectra of $CuCo_2O_4$ samples heat-treated at different temperature. All the diffraction peaks of the $CuCo_2O_4$-450 at 19.1º, 31.3º, 37.0º, 59.6º and 65.7º are associated to the (111), (220), (311), (511) and (440) planes of the $CuCo_2O_4$ spinel structure (JCPDS card No. 01-1155). However, the crystallinity of the $CuCo_2O_4$-60 and $CuCo_2O_4$-250 are not good. The $CuCo_2O_4$-250 sample was further investigated using TEM analysis. As shown in Fig. 3b, the $CuCo_2O_4$-250 consists of accumulated nanoparticles. From the HRTEM image shown in Fig. 3c, the diameters of $CuCo_2O_4$ nanoparticles are less than 5 nm. The measured lattice spacing of 0.243 nm and 0.285 nm are corresponding to the (311) and (220) planes of $CuCo_2O_4$-250 nanoparticles. The results of EDX elemental mapping for the $CuCo_2O_4$-250 nanoparticles are shown in Fig. 3d. The Cu, Co and O elements are uniformly

distributed in the sample, and the atom ratio of Cu, Co and O is about 1:2:9. The large amount of O atoms should be due to the –OH species on the surface of $CuCo_2O_4$ nanoparticles. Hence, we can confirm that ultra-fine $CuCo_2O_4$ nanoparticles have been successfully synthesized using the co-precipitation method assisted with $NaBH_4$ and CTAB.at the ambient condition.

Because the solutions of $CoCl_2 \cdot 6H_2O$ and $CuCl_2 \cdot 2H_2O$ are acidic, the $NaBH_4$ was spontaneously and drastically hydrolyzed and H_2 gas was released, based on the chemical reaction listed in equation (3) [35]. Formation of these H_2 gas caused numerous bubbles in the solution due to the usage of CTAB. The hydrolysis product of $NaBO_2$ was further hydrolyzed and an alkaline condition was generated (see equation 3). Meanwhile, Cu^{2+} and Co^{2+} ions were changed into CoCu nanoclusters due to the usages of $NaBH_4$ as shown in equation (5). Due to the presence of both CTAB and H_2 bubbles, the CoCu nanoclusters were formed and their growth was restrained. After the H_2 bubbles were disappeared and oxygen in air was re-dissolved in the solution, the CuCo clusters were then rapidly oxidized into $CuCo_2O_4$ nanoparticles, following the chemical reaction in quation (6).

$$NaBH_4 + 2H_2O \rightarrow NaBO_2 + 4H_2\uparrow \quad (3)$$

$$BO_2^- + 2H_2O \rightarrow B(OH)_3 + OH^- \quad (4)$$

$$Cu^{2+} + 2Co^{2+} + NaBH_4 + 6OH^- \rightarrow Cu + 2Co + NaBO_2 + 4H_2O + H_2\uparrow \quad (5)$$

$$Cu + 2Co + O_2 \rightarrow CuCo_2O_4 \quad (6)$$

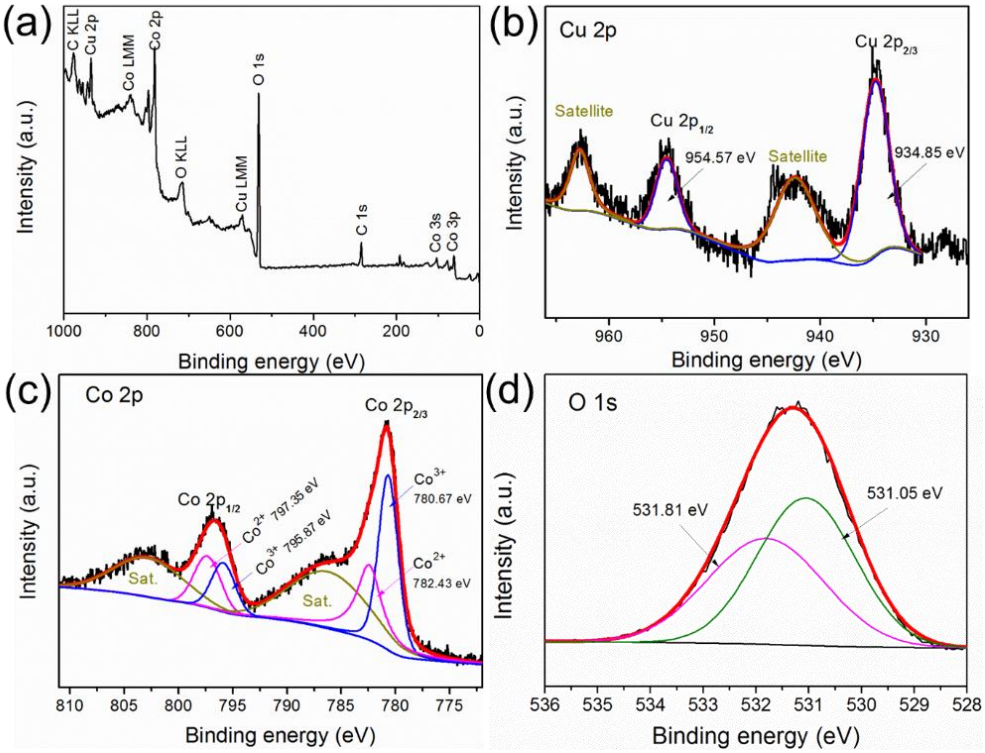

Fig. 4 (a) XPS survey spectrum of the $CuCo_2O_4$-250 nanoparticles; high-resolution XPS spectra of (b) Cu 2p; (c) Co 2p and (d) O 1s.

Chemical states and elemental composition of $CuCo_2O_4$-250 nanoparticles were characterized using XPS. As shown in Fig. 4a, the XPS survey spectrum of $CuCo_2O_4$-250 nanoparticles proves the presence of Cu, Co and O elements. For the high resolution XPS spectra of Cu 2p shown in Fig. 4b, the two peaks at binding energies of 954.57 and 934.85 eV are assigned to Cu $2p_{1/2}$ and Cu $2p_{3/2}$ of Cu^{2+}, respectively. In addition, two satellite peaks also appear at 962.77 and 942.44 eV, confirming the Cu^{2+} characteristics [36]. There are two spin-orbit doublets and two satellites in the high-resolution XPS spectrum of Co 2p as shown in Fig 4c. The spin-energy separation between Co $2p_{1/2}$ and Co $2p_{3/2}$ is ~15 eV. The deconvoluted peaks at 795.87 and 780.67 eV are attributed to Co $2p_{1/2}$ and Co $2p_{3/2}$ of Co^{3+} [37], and the deconvoluted peaks at 797.35 and 782.43 eV are attributed to Co $2p_{1/2}$ and Co $2p_{3/2}$ of Co^{2+} [38], confirming

the presence of Co^{2+} and Co^{3+} in the $CuCo_2O_4$-250 nanoparticles. The high-resolution O 1s spectrum is shown in Fig. 4d and can be deconvoluted into two peaks, which correspond to two type oxygen species. The peak at 531.05 eV is corresponding to the lattice oxygen atoms of $CuCo_2O_4$-250, and the peak at 531.81 eV is corresponding to oxygen defect sites [39, 40].

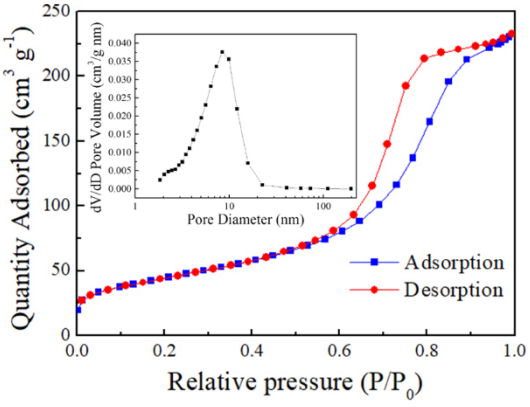

Fig. 5 N_2 adsorption/desorption isotherm of $CuCo_2O_4$-250 nanoparticles (inset shows the pore size distributions)

Porous structure and BET surface area of the $CuCo_2O_4$-250 were further investigated based on the N_2 adsorption-desorption isotherm. As shown in Fig. 5, the obtained curve shows a type-IV isotherm characteristic with a hysteresis loops [41], indicating formation of mesoporous structure. The pore sizes are ranged from 2 nm to 20 nm and mainly centered at ~8.5 nm with a large pore volume of 0.3599 $cm^3 g^{-1}$ (see the inset in Fig. 5). The formation of mesoporous structures should be resulted from the accumulation of $CuCo_2O_4$-250 nanoparticles. Because of the ultra-fine size and large porosity, the $CuCo_2O_4$-250 nanoparticles show a large BET surface area of 159.6 $m^2 g^{-1}$. Therefore, the ultra-fine nanoparticle morphology, large surface area and large porosity of the $CuCo_2O_4$-250 nanoparticles provide abundant active sites on their

surfaces and lots of good pathways for electrolyte ions. These are beneficial to the faradic reactions in charging/discharging process for the supercapacitor electrode material, thus resulting in a high specific capacity.

3.3 Electrochemical properties of $CuCo_2O_4$-250 nanoparticles based electrodes

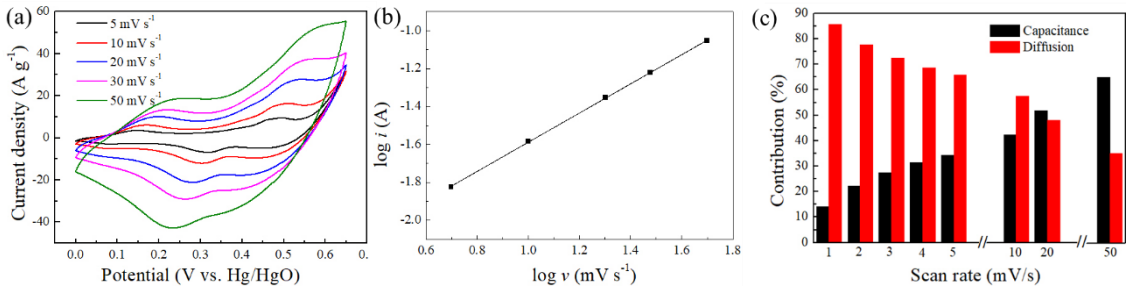

Fig. 6 (a) CV curves of $CuCo_2O_4$-250 nanoparticles based electrode at different scan rates, (b) the logarithm relationships between anodic peak and scan rate and (c) capacitance and diffusion contribution of $CuCo_2O_4$-250 electrode in the charging/discharging processes

CV curves of $CuCo_2O_4$-250 nanoparticles based electrodes were measured at different scan rates and the obtained results are shown in Fig. 6a. There are small redox peaks in all CV curves, which should be attributed to the following reversible redox reactions on the electrode active materials during charging/discharging processes [21, 42]:

$$CuCo_2O_4 + OH^- + H_2O \leftrightarrow CuOOH + 2CoOOH + e^- \quad (7)$$

$$CoOOH + OH^- \leftrightarrow CoO_2 + H_2O + e^- \quad (8)$$

$$CuOOH + OH^- \leftrightarrow CuO + H_2O + e^- \quad (9)$$

It should be noted that these redox peaks gradually decrease with the increase of scanning rate, which might indicate that these redox reactions are not predominant any more during charge/discharge processes in the process of increasing the scanning rate

[43]. The electrochemical reaction kinetics on electrode can be described using the following formula [44]:

$$i=av^{b} \quad (10)$$

where i is the redox peak current (A), and v is scan rate (mV s^{-1}) from the CV curves in Fig. 6a. 'a' and 'b' are adjustable parameters, which are determined by the intercept and slope of log (v)−log (i) plot. The b-value can be used to explain the energy storage behavior of active materials. If the b value is 1, it indicates that the electrochemical active materials are totally capacitive-type behavior based on a fast surface-controlled Faradic process. Whereas if the b value is 0.5, it indicates that the materials have a diffusion controlled battery-type characteristic based on the ion semi-infinite diffusion process [45]. In this study, the b-value calculated from the log (v)−log (i) plot of the $CuCo_2O_4$-250 nanoparticle electrode is 0.77 (see Fig. 6b). The obtained large b-value indicates that there are mixed battery-type behavior and capacitive-type behavior in charging/discharging process. Furthermore, the contribution of the surface capacitive-type behavior ($k_1 v$) and the battery-type diffusion-control behavior ($k_2 v^{0.5}$) can be described using the equation (11) [46, 47]:

$$i\,(V) = k_1 v + k_2 v^{0.5} \quad (11)$$

where k_1 and k_2 are constant, which can be obtained from the fitting plots of $i/v^{0.5}$ versus $k_2 v^{0.5}$. From the CV curves of $CuCo_2O_4$-250 nanoparticle electrode, the obtained percentage of capacitance contributions ($k_1 v$) as shown in Fig. 6c are 14.2%, 22.3%, 27.5%, 31.3%, 34.2%, 42.4%, 51.9% and 64.9% at the scan rate of 1, 2, 3, 4, 5, 10, 20, 50 mV s^{-1} respectively. These further prove that there are the surface capacitive-type

behavior and the battery-type diffusion-control behavior in the charging/discharging processes. Therefore, although $CuCo_2O_4$ is reported as a typical battery-type material in literature [30-32, 48], the $CuCo_2O_4$-250 nanoparticles in this study show a mixed behavior due to their ultra-fine sizes, large specific surface area and large pore volumes.

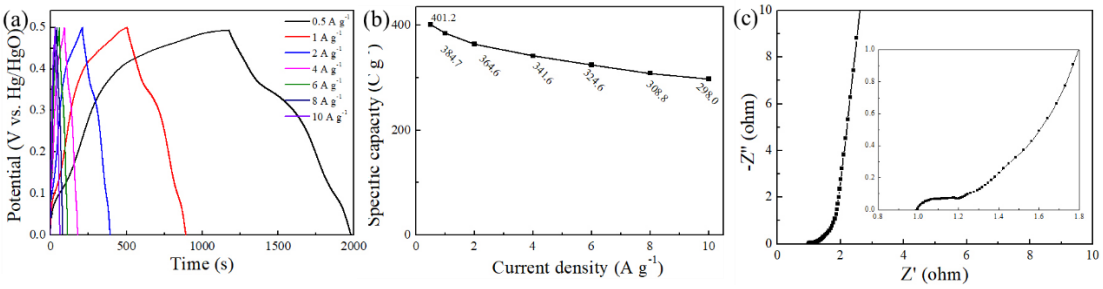

Fig. 7 (a) GCD curves and (b) specific capacities of the $CuCo_2O_4$-250 nanoparticle electrode at different current densities; (c) Nyquist plots of the $CuCo_2O_4$-250 nanoparticle electrode.

Fig. 7a shows the GCD curves of the $CuCo_2O_4$-250 nanoparticle electrode at various current densities within a potential range of 0 ~ 0.5 V. It is well known that the plateaus in the GCD curves is attributed to the reversible redox reactions for a typical battery-type behavior during charging/discharging processes. However, there are only very small plateaus in these discharging processes from the GCD curves of $CuCo_2O_4$-250 nanoparticle electrode in Fig. 7a, suggesting that the capacity is contributed from both surface capacitive-type effect and diffusion controlled battery-type during the whole process [44].

As shown in Fig. 7b, the calculated specific capacity values of the $CuCo_2O_4$-250 nanoparticles based on the GCD curves are 401.2, 384.7, 364.6, 341.6, 324.6, 308.8 and 298.0 C g^{-1} at 0.5, 1, 2, 4, 6, 8 and 10 A g^{-1} respectively. Results show that the $CuCo_2O_4$ nanoparticle electrode can maintain 77.5% of capacitance from 1 A g^{-1} to a

large current density of 10 A g^{-1}, suggesting its excellent rate capability. Therefore, the $CuCo_2O_4$ nanoparticle electrode has not only high specific values, but also a high rate capability. Compared to other $CuCo_2O_4$ electrodes reported in literature as listed in Table 1, the $CuCo_2O_4$-250 nanoparticle electrode in this study displays a higher specific capacitance and a better rate capability than those of $CuCo_2O_4$ nanostructure based electrodes, such as nanobelts [9], nanoparticles [33, 48], nanowires [27], nanoflowers [32], nanoneedles [30], hollow microspheres [31] and chrysanthemum-like $CuCo_2O_4$ [49]. The high specific capacity should be attributed to the large specific area and pore volume, which lead to a fast Faradic process and a high ion diffusion rate. Furthermore, at high current densities, the electrolyte ions can sufficiently diffuse onto the surface of $CuCo_2O_4$-250 nanoparticles and react with the active sites, thus maintaining a high specific capacity.

Table 1. Summary of electrochemical properties of other $CuCo_2O_4$ electrodes coated on current collector using as-prepared samples in literature.

Materials	**Method**	**Rate Capability**	**BET (m^2 g^{-1})**	**Specific Capacity**	**Ref**
$CuCo_2O_4$ nanobelts	Hydrothermal	23% (1.46/10.7 A/g)	33.43	809 F/g at 0.667 A/g	[9]
$CuCo_2O_4$ nanoparticles	Hydrothermal	36.9% (2/10 A/g)	133	765 F/g at 1A/g	[48]
$CuCo_2O_4$ hollow microspheres	Hydrothermal	68% (1/20 A/g)	42.5	691 F/g at 1 A/g	[31]
$CuCo_2O_4$ nanoparticles	Hydrothermal	54% (0.4/2 A/g)	-	206 C/g at 0.4 A/g	[33]
PANI/ $CuCo_2O_4$ composite	Hydrothermal	32% (0.4/2 A/g)	-	403 C/g at 0.4 A/g	[33]
$CuCo_2O_4$ nanoflowers	Hydrothermal.	40% (1/20 A/g)	157	202.8 C/g at 1 A/g	[32]
$CuCo_2O_4$ octahedrons	Hydrothermal	40% (2/10 A/g)	61.97	338 C/g at 2 mV/s	[28]
$CuCo_2O_4$ nanoneedle arrays	Hydrothermal	-	-	390 F/g at 0.5 A/g	[30]
Chrysanthemum-like $CuCo_2O_4$	Hydrothermal	71.3% (0.5/15A/g)	24.18	335.8 F/g at 0.5 A/g	[49]
Porous $CuCo_2O_4$ nanowires	Electrospinning	41.2% (1/15mA/cm^2)	-	443.9 mF/cm^2 at 1 mA/cm^2	[27]
$CuCo_2O_4$ nanoparticles	Co-precipitation	77.5%(1/10A/g)	159.6	401.2 C/g at 0.5 A/g	This work

EIS measurement was carried out to further investigate the electrochemical properties. Fig. 7c shows the corresponding Nyquist plots of the $CuCo_2O_4$ nanoparticle electrodes, all of which consist of three distinct regions, including a linear section at the low frequency range, a real axis intercept and a semicircle in the high frequency range. The real axis intercept suggests that the equivalent series resistance (ESR, R_s) [50], is the combination of the ionic resistance of electrolyte, the intrinsic resistance of active materials, and the interface resistance between current collector and active material. The diameter of the semicircle corresponds to the Faradic resistance (R_{ct}) of the redox reactions on electrodes [4, 50]. The slope of the line at the low frequency range represents the Warburg resistance (R_w) for the diffusion processes [4]. It is well-known that an ideal pseudo-capacitance materials should display a very small semicircle followed by ~90° straight line, while a typical battery material should have a much larger semicircle than a pseudo-capacitance material followed by a 45° straight line [51]. From the plots, the $CuCo_2O_4$ nanoparticles electrodes show much smaller semicircle diameter and nearly vertical line, indicating its pseudo-capacitance behavior. The $CuCo_2O_4$ nanoparticle electrodes possess very small R_s vales (0.98 Ω) and R_{ct} (0.27 Ω), implying the very fast Faradic process and ion diffusion rate.

3.4 Electrochemical performance of $CuCo_2O_4$-250//AC asymmetric supercapacitor

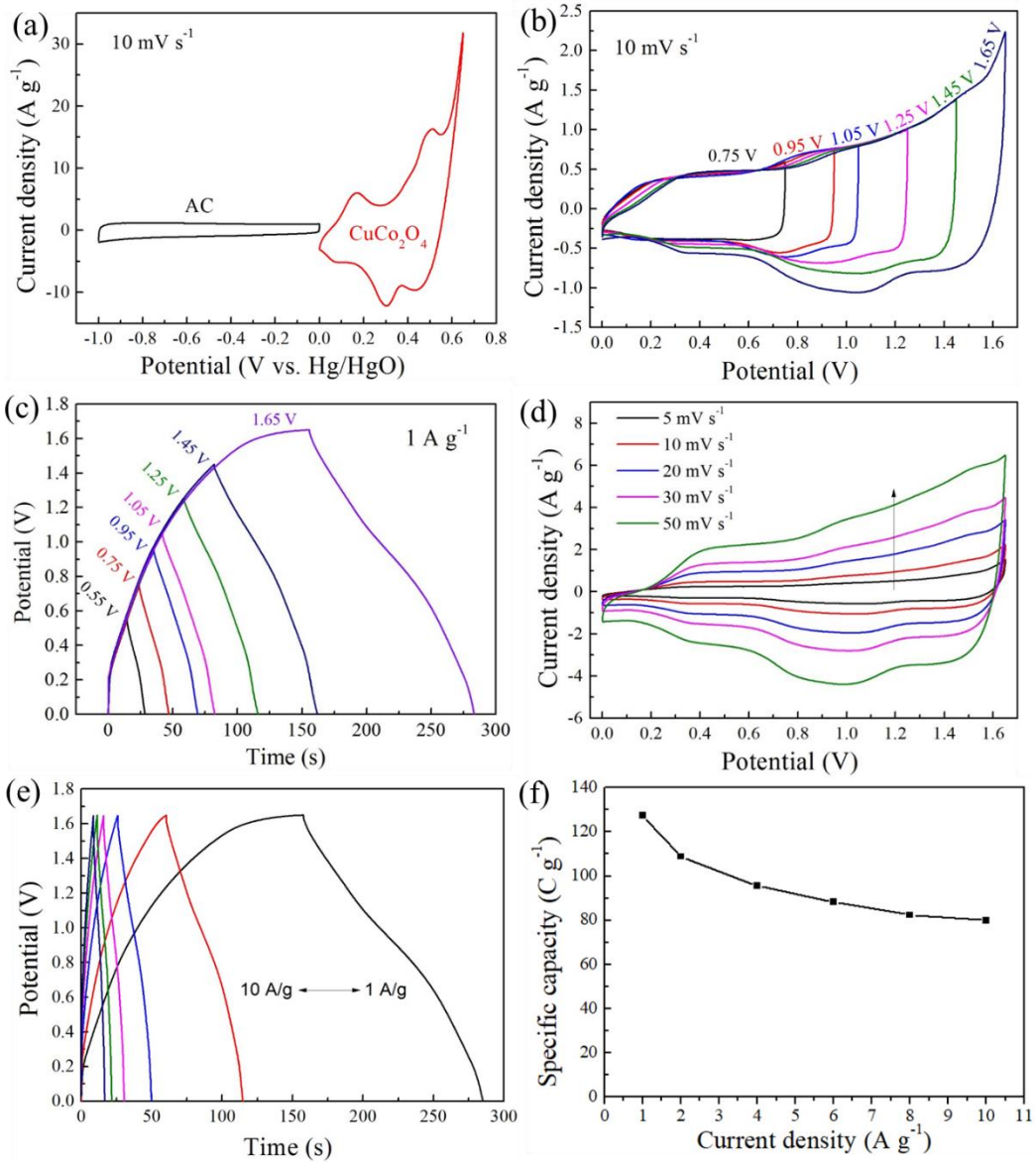

Fig. 8 Electrochemical performance of $CuCo_2O_4$-250//AC asymmetric supercapacitor. (a) CV curves of $CuCo_2O_4$-250 nanoparticles and active carbon at 10 mV s^{-1}; (b) CV curves and (c) GCD curves of $CuCo_2O_4$-250//AC ASC at various potential windows; (d) CV curves of $CuCo_2O_4$-250//AC ASC at various scan rates; (e) GCD curves and (f) corresponding specific capacitance value of the $CuCo_2O_4$-250//AC ASC at various current densities.

An asymmetric supercapacitor (ASC) of $CuCo_2O_4$-250//AC was built up and its electrochemical properties are presented in Fig. 8. Fig. 8a displays the CV profiles of

$CuCo_2O_4$-250 nanoparticles (positive electrode) and AC (negative electrode) at a scan rate of 10 mV s^{-1}, which were obtained within the potential ranges of -1 ~ 0 V and 0 ~ 0.65 V for $CuCo_2O_4$-250 nanoparticles and AC electrodes, respectively. Results show that the potential range of the ASC device is as large as 1.65 V [52]. Figs. 8b and 8c display the CV and GCD curves of the $CuCo_2O_4$-250 nanoparticles//AC in different potential window. The ACS device is quite stable in the potential window less than 1.65 V, thus we can assume the suitable operation potential window for the $CuCo_2O_4$-250//AC is ranged from 0 ~ 1.65 V. Fig. 8d displays the CV curves of the $CuCo_2O_4$-250//AC at different scan rates. There are distorted rectangular shapes of curves but without apparent distinct changes in the general shapes in all CV curves, indicating that the ACS device shows a pseudocapacitor property and a good reversibility. Based on the GCD curves of the $CuCo_2O_4$-250//AC obtained at different current densities (see Fig. 8e), the specific capacities (C_d, C/g) can be obtained by the following formula (12) [53]:

$$C_d = \frac{I \times \Delta t}{M} \tag{12}$$

where I is the measured current (mA), Δt is the discharge time (s), M (mg) are the total mass of active materials of $CuCo_2O_4$-250 nanoparticles and AC.. As shown in Fig. 8f, the obtained capacitances of the $CuCo_2O_4$-250//AC is 127.4 C g^{-1} at 1 A g^{-1}, and still maintain a value of 80.0 C g^{-1} at a high rate of 10 A g^{-1}.

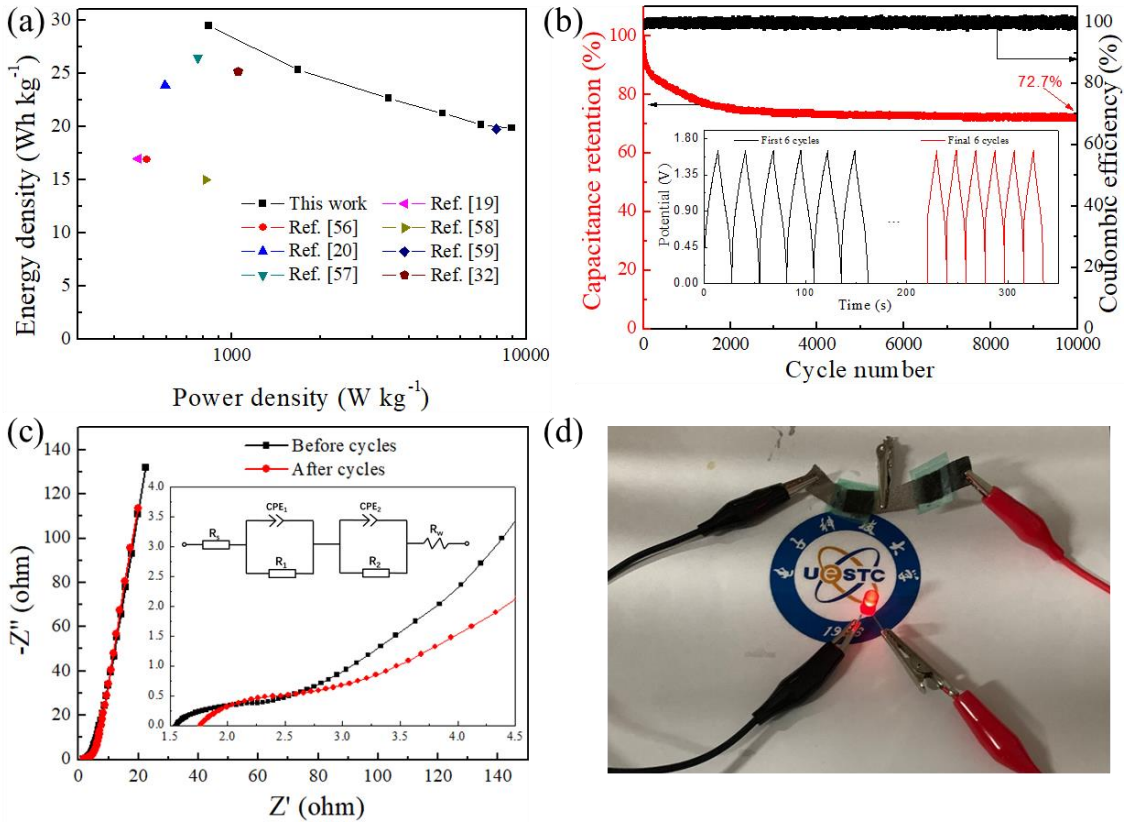

Fig. 9 (a) Ragone plots; (b) cycling performance (inset is GCD curves of first and last 6 cycles); (c) Nyquist plots (inset: the corresponding equivalent circuit) and (d) lighted LED bulb using the $CuCo_2O_4$-250//AC ASC.

The energy density (E, Wh kg^{-1}) and power density (P, W kg^{-1}) of the $CuCo_2O_4$-250//AC were then calculated using the specific capacity (C_d), potential window ΔV and discharge time (Δt) based on the formula (13) and (14) [52, 54]:

$$E = \frac{C_d \times \Delta V}{2 \times 3600} \tag{13}$$

$$P = \frac{E \times 3600}{\Delta t} \tag{14}$$

Based on the obtained energy and power density at various current densities, the obtained Ragone plots of the $CuCo_2O_4$-250//AC are represented in Fig. 9a. The $CuCo_2O_4$-250//AC shows a high energy density of 29.5 Wh kg^{-1} at a power density of 832.6 W kg^{-1}, and maintain 19.9 Wh kg^{-1} at 8943.8 W kg^{-1}, which are higher than many

reported data of $CuCo_2O_4$-250//AC devices, for example, maguey-like $CuCo_2O_4$ nanowires//AC (16.9 Wh kg^{-1} at 513 W kg^{-1}) [53], $CuCo_2O_4$ nanourchin//AC (23.9 Wh kg^{-1} at 593.2 W kg^{-1}) [19], cedar leaf-like $CuCo_2O_4$//AC (26.5 Wh kg^{-1} at 763.8 W kg^{-1}) [55], ordered corn-like $CuCo_2O_4$ nanoforests//AC (17 Wh kg^{-1} at 480 W kg^{-1}) [18], $NiCo_2O_4$ nanosheets/$CuCo_2O_4$ nanocones//AC (15 Wh kg^{-1} at 814 W kg^{-1}) [56], $CuCo_2O_4$//AC (25 Wh kg^{-1} at 450 W kg^{-1}) [48], triple-shelled hollow $CuCo_2O_4$//AC (25.2 Wh kg^{-1} at 1050 W kg^{-1}) [31].

The cyclic stability of the $CuCo_2O_4$-250//AC was further tested at 6 A g^{-1} for 10,000 cycles, and the obtained results are shown in Fig. 9b. The shape of GCD curves has not been apparently changed before and after cycling test. The capacity of the $CuCo_2O_4$-250//AC device retains 72.7% of its initial value even after 10,000 cycles. The capacity reduction of this device occurred mainly in the first 1000 cycles, which retains about 80.0%. During the whole cycling test, the Coulombic efficiency is maintained as high as 99.5%. The EIS tests of the $CuCo_2O_4$//AC before and after cycling test were performed, and the obtaind Nyquist plots of the $CuCo_2O_4$-250//AC ASC are shown in Fig. 9c and the impedance data can be simulated and analyzed. CPE_1 and CPE_2 represent the non-ideal state of the surface of negative and positive electrodes, respectively. R_1 and R_2 are the Faradic resistance of the redox reactions on negative and positive electrodes, respectively. R_w is Warburg resistance for the diffusion processes and R_s is the ESR. From the plots, the $CuCo_2O_4$-250//AC ASC show a much smaller semicircle diameter and nearly a vertical line, indicating its pseudo-capacitance behavior. With the cycles increased, ohmage and charge transfer impedance are

enlarged slightly and there is no obvious change in diffusion impedance. Thus, the total impedance shows an increasing trend. The plots still show small values of R_s (1.77 Ω) and R_{ct} (1.30 Ω) after 10,000 cycles indicating that the $CuCo_2O_4$-250//AC maintains a good performance after long-term charges/discharge processes.

4 Conclusions

$CuCo_2O_4$ nanoparticles were successfully synthesized in this study using a facile co-precipitation method. Attributed to their small sizes, large specific surface areas, larger pore volumes and abundant active sites, these $CuCo_2O_4$ nanoparticles based electrode exhibited high specific capacitance and good rate capability. It showed a mixed battery-type behavior with a diffusion-control process and a capacitive-type behavior with surface capacitive effect in charging/discharging processes. An assembled $CuCo_2O_4$-250//AC ASC achieved a high energy density of 29.5 Wh kg^{-1} at a power density of 832.6 W kg^{-1}, and its capacitance remained 72.7% after 10000 charge/discharge cycles. Therefore, the room temperature synthesized $CuCo_2O_4$ nanoparticles could be applied as good electrodes for energy storage devices with excellent electrochemical performance.

Acknowledgments

This work is supported by International Exchange Grant (IEC/NSFC/201078) through Royal Society and the National Natural Science Foundation of China (NSFC).

References

[1] W. Raza, F. Ali, N. Raza, Y. Luo, K.-H. Kim, J. Yang, S. Kumar, A. Mehmood, E.E. Kwon, Recent advancements in supercapacitor technology, Nano Energy, 52 (2018) 441-473.

[2] W. Liu, S. Zhang, S.U. Dar, Y. Zhao, R. Akram, X. Zhang, S. Jin, Z. Wu, D. Wu, Polyphosphazene-derived heteroatoms-doped carbon materials for supercapacitor electrodes, Carbon, 129 (2018) 420-427.

[3] A. Rudge, I. Raistrick, S. Gottesfeld, J.P. Ferraris, A study of the electrochemical properties of conducting polymers for application in electrochemical capacitors, Electrochim. Acta, 39 (1994) 273-287.

[4] M. Chuai, X. Chen, K. Zhang, J. Zhang, M. Zhang, CuO–SnO_2 reverse cubic heterojunctions as high-performance supercapacitor electrodes, J. Mater. Chem. A, 7 (2019) 1160-1167.

[5] J. Wan, A. Pang, D. He, J. Liu, H. Suo, C. Zhao, A high-performance supercapacitor electrode based on three-dimensional poly-rowed copper hydroxide nanorods on copper foam, J. Mater. Sci. : Mater. El., 29 (2017) 2660-2667.

[6] Y. Sui, H. Hu, J. Qi, Y. Zhou, F. Wei, Y. He, Q. Meng, Y. Ren, Z. Sun, Facile synthesis of $Cu_{1.96}S$ nanoparticles for enhanced energy density in flexible all-solid-state asymmetric supercapacitors, J. Mater. Sci. : Mater. El., 29 (2018) 11187-11198.

[7] P. Siwatch, K. Sharma, S.K. Tripathi, Facile synthesis of $NiCo_2O_4$ quantum dots for asymmetric supercapacitor, Electrochim. Acta, 329 (2020).

[8] Y.Y. Zhang, J.X. Wang, J.H. Ye, P.P. Wan, H.M. Wei, S.Q. Zhao, T.F. Li, S. Hussain,

$NiCo_2O_4$ arrays nanostructures on nickel foam: Morphology control and application for pseudocapacitors, Ceram. Int., 42 (2016) 14976-14983.

[9] S. Vijayakumar, S.-H. Lee, K.-S. Ryu, Hierarchical $CuCo_2O_4$ nanobelts as a supercapacitor electrode with high areal and specific capacitance, Electrochim. Acta, 182 (2015) 979-986.

[10] Y. Gao, Y. Xia, H. Wan, X. Xu, S. Jiang, Enhanced cycle performance of hierarchical porous sphere $MnCo_2O_4$ for asymmetric supercapacitors, Electrochim. Acta, 301 (2019) 294-303.

[11] J. Li, D. Xiong, L. Wang, M.K.S. Hirbod, X. Li, High-performance self-assembly $MnCo_2O_4$ nanosheets for asymmetric supercapacitors, J. Energy Chem., 37 (2019) 66-72.

[12] H. Chen, J. Wang, X. Han, F. Liao, Y. Zhang, L. Gao, C. Xu, Facile synthesis of mesoporous $ZnCo_2O_4$ hierarchical microspheres and their excellent supercapacitor performance, Ceram. Int., 45 (2019) 8577-8584.

[13] Y.A. Kumar, K.D. Kumar, H.-J. Kim, Reagents assisted $ZnCo_2O_4$ nanomaterial for supercapacitor application, Electrochim. Acta, 330 (2020).

[14] L.Y. Lin, M.C. Huang, M.L. Ning, K.W. Wu, H.W. Li, S. Hussain, S.Q. Zhao, Facile ordered $ZnCo_2O_4$@MnO_2 nanosheet arrays for superior-performance supercapacitor electrode, Solid State Sci., 84 (2018) 51-56.

[15] K. Xu, S. Ma, Y. Shen, Q. Ren, J. Yang, X. Chen, J. Hu, $CuCo_2O_4$ nanowire arrays wrapped in metal oxide nanosheets as hierarchical multicomponent electrodes for supercapacitors, Chem. Eng. J., 369 (2019) 363-369.

[16] Q. Gao, J. Wang, J. Wang, Morphology-controllable synthesis of $CuCo_2O_4$ arrays on Ni foam as advanced electrodes for supercapacitors, J. Alloy. Compd., 789 (2019) 193-200.

[17] C. Wang, K. Guo, W. He, X. Deng, P. Hou, F. Zhuge, X. Xu, T. Zhai, Hierarchical CuCo2O4@nickel-cobalt hydroxides core/shell nanoarchitectures for high-performance hybrid supercapacitors, Sci. Bull., 62 (2017) 1122-1131.

[18] Y. Wang, D. Yang, J. Lian, T. Wei, Y. Sun, Ordered corn-like $CuCo_2O_4$ nanoforests covering Ni foam for a high-performance all-solid-state supercapacitor, J. Alloy. Compd., 741 (2018) 527-531.

[19] W. Liu, Y. Feng, L. Sun, Y. Zhang, G. Wang, L. Zhao, M. Meng, J. Li, K. Liu, Hierarchical $CuCo_2O_4$ nanourchin supported by Ni foam with superior electrochemical performance, J. Alloy. Compd., 756 (2018) 68-75.

[20] S. Vijayakumar, S. Nagamuthu, K.-S. Ryu, $CuCo_2O_4$ flowers/Ni-foam architecture as a battery type positive electrode for high performance hybrid supercapacitor applications, Electrochim. Acta, 238 (2017) 99-106.

[21] S.M. Pawar, B.S. Pawar, P.T. Babar, A.T.A. Ahmed, H.S. Chavan, Y. Jo, S. Cho, J. Kim, B. Hou, A.I. Inamdar, S. Cha, J.H. Kim, T.G. Kim, H. Kim, H. Im, Nanoporous $CuCo_2O_4$ nanosheets as a highly efficient bifunctional electrode for supercapacitors and water oxidation catalysis, Appl. Surf. Sci., 470 (2019) 360-367.

[22] L. Abbasi, M. Arvand, Engineering hierarchical ultrathin $CuCo_2O_4$ nanosheets array on Ni foam by rapid electrodeposition method toward high-performance binder-free supercapacitors, Appl. Surf. Sci., 445 (2018) 272-280.

[23] X. Liang, Q. Wang, Y. Ma, D. Zhang, A high performance asymmetric supercapacitor based on in situ prepared $CuCo_2O_4$ nanowires and PPy nanoparticles on a two-ply carbon nanotube yarn, Dalton T., 47 (2018) 17146-17152.

[24] X. Liu, E.H. Yu, K. Scott, Preparation and evaluation of a highly stable palladium yttrium platinum core–shell–shell structure catalyst for oxygen reduction reactions, Applied Catalysis B: Environmental, 162 (2015) 593-601.

[25] L. Zhang, X. Ji, X. Wang, Y. Fu, H. Zhu, T.X. Liu, Chemically Ordered Pt–Co–Cu/C as Excellent Electrochemical Catalyst for Oxygen Reduction Reaction, J. Electrochem. Soc., 167 (2020) 024507.

[26] S. Liu, K.S. Hui, K.N. Hui, J.M. Yun, K.H. Kim, Vertically stacked bilayer $CuCo_2O_4$/$MnCo_2O_4$ heterostructures on functionalized graphite paper for high-performance electrochemical capacitors, J. Mater. Chem. A, 4 (2016) 8061-8071.

[27] Q. Wang, D. Chen, D. Zhang, Electrospun porous $CuCo_2O_4$ nanowire network electrode for asymmetric supercapacitors, RSC Adv., 5 (2015) 96448-96454.

[28] A.K. Das, N.H. Kim, S.H. Lee, Y. Sohn, J.H. Lee, Facile synthesis of $CuCo_2O_4$ composite octahedrons for high performance supercapacitor application, Compos. Part B-Eng., 150 (2018) 269-276.

[29] X. Liu, J. Xi, B.B. Xu, B. Fang, Y. Wang, M. Bayati, K. Scott, C. Gao, A High-Performance Direct Methanol Fuel Cell Technology Enabled by Mediating High-Concentration Methanol through a Graphene Aerogel, Small Methods, 2 (2018) 1800138.

[30] J. Qi, D. Chen, W. Wang, Y. Sui, Y. He, Q. Meng, F. Wei, Y. Ren, J. Liu, Y. Jin,

Facile synthesis of N-doped activated carbon derived from cotton and $CuCo_2O_4$ nanoneedle arrays electrodes for all-solid-state asymmetric supercapacitor, J. Mater. Sci.-Materials in Electronics, 30 (2019) 9877-9887.

[31] G. Li, S. Liu, Y. Pan, T. Zhou, J. Ding, Y. Sun, Y. Wang, Self-templated formation of $CuCo_2O_4$ triple-shelled hollow microspheres for all-solid-state asymmetric supercapacitors, J. Alloy. Compd., 787 (2019) 694-699.

[32] X. Xu, Y. Liu, P. Dong, P.M. Ajayan, J. Shen, M. Ye, Mesostructured $CuCo_2S_4$/$CuCo_2O_4$ nanoflowers as advanced electrodes for asymmetric supercapacitors, J. Power Sources, 400 (2018) 96-103.

[33] F.S. Omar, A. Numan, N. Duraisamy, M.M. Ramly, K. Ramesh, S. Ramesh, Binary composite of polyaniline/copper cobaltite for high performance asymmetric supercapacitor application, Electrochim. Acta, 227 (2017) 41-48.

[34] H. Li, Z. Li, Z. Wu, M. Sun, S. Han, C. Cai, W. Shen, Y. Fu, Nanocomposites of Cobalt Sulfide Embedded Carbon Nanotubes with Enhanced Supercapacitor Performance, J. Electrochem. Soc., 166 (2019) A1031-A1037.

[35] Y. Zhou, Y. Wu, P. Zhang, J. Chen, B. Qu, J.T. Li, Co_3O_4@(Fe-Doped)$Co(OH)_2$ Microfibers: Facile Synthesis, Oriented-Assembly, Formation Mechanism, and High Electrocatalytic Activity, ACS Appl. Mater. Inter., 9 (2017) 30880-30890.

[36] H. Yan, Y. Lu, K. Zhu, T. Peng, X. Liu, Y. Liu, Y. Luo, Growth of highly mesoporous $CuCo_2O_4$@C core-shell arrays as advanced electrodes for high-performance supercapacitors, Appl. Surf. Sci., 439 (2018) 883-890.

[37] D. Wu, R. Jia, M. Wen, S. Zhong, Q. Wu, S. Yu, Y. Fu, Ultra-stable hyperstructure

of PtCo/Co_3O_4-SiO_2-nanosheet with Active Lattice Oxygen for Superior Catalytic Activity towards CO Oxidation, Inorg chem., 59 (2020) 1218-1226.

[38] A.A. Ensafi, S.E. Moosavifard, B. Rezaei, S.K. Kaverlavani, Engineering onion-like nanoporous $CuCo_2O_4$ hollow spheres derived from bimetal-organic frameworks for high-performance asymmetric supercapacitors, J. Mater. Chem. A, 6 (2018) 10497-10506.

[39] Y. Zeng, Z. Lai, Y. Han, H. Zhang, S. Xie, X. Lu, Oxygen-vacancy and surface modulation of ultrathin nickel cobaltite nanosheets as a high-energy cathode for advanced zn-ion batteries, Adv Mater, (2018) e1802396.

[40] J. Hao, S. Peng, H. Li, S. Dang, T. Qin, Y. Wen, J. Huang, F. Ma, D. Gao, F. Li, G. Cao, A low crystallinity oxygen-vacancy-rich Co_3O_4 cathode for high-performance flexible asymmetric supercapacitors, J. Mater. Chem. A, 6 (2018) 16094-16100.

[41] K.H. Juan Xu, Zhengwei Ju, Chaojie Ma, Wenchang Wang, Cheng Wang, Jianyu Cao, and Zhidong Chen, Synthesis and Electrochemical Properties of Carbon Dots/Manganese Dioxide (CQDs/MnO_2) Nanoflowers for Supercapacitor Applications, J. Electrochem. Soc., 164 (2017) A430-A437.

[42] S. Cheng, S. DelaCruz, C. Chen, Z. Tang, T. Shi, C. Carraro, R. Maboudian, Hierarchical Co_3O_4/CuO nanorod array supported on carbon cloth for highly sensitive non-enzymatic glucose biosensing, Sensors and Actuators B-Chemical, 298 (2019).

[43] Q. Zong, H. Yang, Q. Wang, Q. Zhang, Y. Zhu, H. Wang, Q. Shen, Three-dimensional coral-like NiCoP@C@$Ni(OH)_2$ core-shell nanoarrays as battery-type electrodes to enhance cycle stability and energy density for hybrid supercapacitors,

Chem. Eng. J., 361 (2019) 1-11.

[44] B. Kirubasankar, P. Palanisamy, S. Arunachalam, V. Murugadoss, S. Angaiah, 2D MoSe2-Ni(OH)$_2$ nanohybrid as an efficient electrode material with high rate capability for asymmetric supercapacitor applications, Chem. Eng. J., 355 (2019) 881-890.

[45] F. Yu, T. Huang, P. Zhang, Y. Tao, F.-Z. Cui, Q. Xie, S. Yao, F. Wang, Design and synthesis of electrode materials with both battery-type and capacitive charge storage, Energy Storage Mater., 22 (2019) 235-255.

[46] G.A. Muller, J.B. Cook, H.S. Kim, S.H. Tolbert, B. Dunn, High performance pseudocapacitor based on 2D layered metal chalcogenide nanocrystals, Nano Lett., 15 (2015) 1911-1917.

[47] J. Wang, J. Polleux, J. Lim, B. Dunn, Pseudocapacitive contributions to electrochemical energy storage in TiO_2 (anatase) nanoparticles, J. Phys. Chem. C, 111 (2007) 14925-14931.

[48] R. BoopathiRaja, M. Parthibavarman, A.N. Begum, Hydrothermal induced novel $CuCo_2O_4$ electrode for high performance supercapacitor applications, Vacuum, 165 (2019) 96-104.

[49] Y.-q. Zhao, Y. Zhang, K.-z. Xu, Effect of Precursor on the Morphology and Supercapacitor Performance of $CuCo_2O_4$, Int. J. Electrochem. Sci., 14 (2019) 3885-3896.

[50] Z. Zhang, H. Wang, Y. Zhang, X. Mu, B. Huang, J. Du, J. Zhou, X. Pan, E. Xie, Carbon nanotube/hematite core/shell nanowires on carbon cloth for supercapacitor anode with ultrahigh specific capacitance and superb cycling stability, Chem. Eng. J.,

325 (2017) 221-228.

[51] J. Xie, P. Yang, Y. Wang, T. Qi, Y. Lei, C.M. Li, Puzzles and confusions in supercapacitor and battery: Theory and solutions, J. Power Sources, 401 (2018) 213-223.

[52] H. Li, Z. Li, M. Sun, Z. Wu, W. Shen, Y.Q. Fu, Zinc cobalt sulfide nanoparticles as high performance electrode material for asymmetric supercapacitor, Electrochim. Acta, 319 (2019) 716-726.

[53] L. Liao, H. Zhang, W. Li, X. Huang, Z. Xiao, K. Xu, J. Yang, R. Zou, J. Hu, Facile synthesis of maguey-like $CuCo_2O_4$ nanowires with high areal capacitance for supercapacitors, J. Alloy. Compd., 695 (2017) 3503-3510.

[54] H. Li, Z. Li, Z. Wu, M. Sun, S. Han, C. Cai, W. Shen, X. Liu, Y. Fu, Enhanced electrochemical performance of $CuCo_2S_4$/carbon nanotubes composite as electrode material for supercapacitors, J. Colloid. Interf. Sci., 549 (2019) 105-113.

[55] Y. Wang, D. Yang, J. Lian, J. Pan, T. Wei, Y. Sun, Cedar leaf-like CuCo2O4 directly grow on nickel foam by a hydrothermal/annealing process as an electrode for a high-performance symmetric supercapacitor, J. Alloy. Compd., 735 (2018) 2046-2052.

[56] S. Wen, Y. Liu, H. Bai, R. Shao, W. Xu, W. Shi, Full synergistic effect of hydrothermal $NiCo_2O_4$ nanosheets/$CuCo_2O_4$ nanocones supported on Ni foam for high-performance asymmetric supercapacitors, J. Solid State Chem., 262 (2018) 327-334.